

Near-field Imaging of Optical Resonance Modes in Silicon Metasurfaces Using Photoelectron Microscopy

Alex Boehm¹, Sylvain D. Gennaro^{1,2}, Chloe F. Doiron^{1,2}, Thomas E. Beechem³, Michael B. Sinclair¹, Igal Brener^{1,2}, Raktim Sarma^{1,2}, Taisuke Ohta^{1*}

¹Sandia National Laboratories, Albuquerque, NM 87185

²Center for Integrated Nanotechnologies, Albuquerque, NM 87185

³School of Mechanical Engineering and Birck Nanotechnology Center, Purdue University, West Lafayette, IN 47907

Corresponding author: tohta@sandia.gov

ABSTRACT:

Precise control of light-matter interactions at the nanoscale lies at the heart of nanophotonics. Yet their experimental examination is challenging since the corresponding electromagnetic near-field is often confined within volumes below the resolution of conventional optical microscopy. In this work, we demonstrate that photoelectron emission microscopy (PEEM) can be used to image near-field optical fields of nanophotonic structures with a sub-monolayer potassium surface layer to lower the work function and enable two-photon photoemission using near-infrared illumination. We present concurrent spectroscopy and imaging of the near-field distribution of the resonance modes supported by broken-symmetry silicon metasurfaces. We find that the photoemission signal reveals the wavelength dependent, electric near-field distribution of the optical modes. In addition, the large field of view of PEEM allows us to examine the evolution of the collective modes by monitoring individual resonators near the boundary of the metasurface and deduce that coupling between eight resonators establishes the collective excitations. All told, the high-spatial resolution of this hyperspectral imaging approach, combined with an extended field of view, is valuable for the metrology of collective, non-local optical resonances in nanophotonic systems.

KEYWORDS: near-field imaging, near-field spectroscopy, photoemission electron microscopy (PEEM), Si metasurface, quasi-BIC

A recurring challenge of nanophotonics is to engineer structures designed to confine light within a volume smaller than the wavelength of light. Such tight confinement of electromagnetic fields, along with the Purcell effect enhancing the photonic density of states, can greatly intensify light-matter interactions. Resonant structures such as plasmonic antennas,¹ metasurfaces,² or photonic crystals,³ are known for their ability to manipulate electromagnetic fields efficiently within ultrasmall light-matter interaction volumes, leading to applications in sensing,⁴ imaging,⁵ holography,⁶ nonlinear⁷ and quantum optics.^{8,9} While miniaturization has enabled control of the light-matter interactions with unprecedented precision, it has made metrology of such photonic structures more challenging, as the spatial resolution of conventional optical microscopy is inadequate for examination of the spatial field distribution. Researchers thus rely on far-field reflectance data in conjunction with full-wave electromagnetic simulations, exploit the phase information in spectral interferometric microscopy,¹⁰ use biomarkers in super-resolution microscopy,^{11,12} or develop non-conventional approaches to access near-field information.

The desire to image the near-field of nanophotonic systems has motivated several advances in high-resolution scanning imaging approaches and yielded remarkable results. Scattering-type scanning near-field optical microscopy (sSNOM), for example, records the scattered light off a probe that is scanned along a sample surface.^{13,14} However, the probe's presence often perturbs the photonic mode that is being imaged due to additional near-field interaction.¹⁵ In this aspect, approaches that do not involve excitation or detection mediated by a proximal probe are desirable, as in cathodoluminescence microscopy (CL) or electron energy loss spectroscopy (EELS).^{16,17,18,19} CL relies on rastering a focused electron beam over the sample, which excites photonic modes, and then detects the resulting light emission (*i.e.*, “electron in, photon out”).^{20,21} However, because an electron beam is used to excite the photonic modes, multiple modes are often excited simultaneously making interpretation of the results challenging. Meanwhile, EELS operates in an “electron-in, electron-out” approach. Consequently, excitations in EELS are not bound to optical selection rules, and hence it assesses the light-matter interactions indirectly. Moreover, the photonic excitations in all these scanning approaches are spatially localized to within the probe tip or electron beams' dimension and are temporally discrete (*i.e.*, isolated in time). Thus, whether a linear summation of such isolated excitation events can provide a picture equivalent to far-field light excitation is a point of concern.

In recent years, an alternative near-field imaging technique has been developed called photoelectron emission microscopy (PEEM).^{22,23} PEEM can be seen as the inverse of CL²⁴ where photons excite the sample and electrons are collected.^{25,26} This “photon in, electron out” approach offers numerous advantages: far-field excitation with light, akin to typical optical experimental conditions, provides fine control over the polarization, wavelength, and incident angle of light,²⁷ while preserving the high spatial resolution given by the electron's smaller de-Broglie wavelength.²⁸ Since the photoelectron emission occurs in response to absorption of incident photons, which scales with the electromagnetic field intensity, the PEEM signal is stronger where the electric field is stronger.²⁹ PEEM has been successfully applied to image the near-field distribution of metallic plasmonic nanostructures,^{22,23,26,30,31,32} and, to a smaller extent, photonic modes in a conductive oxide³³ and excited states in organic molecules.^{34,35} To further showcase an applicability of PEEM in photonic systems, we employ this technique for semiconductor metasurfaces, which confine the electromagnetic field within or nearby the volume of the individual resonators as

opposed to plasmonic nanostructures, where electromagnetic fields are concentrated at the metal-dielectric interface. Whether photoemission yield is sensitive to the electric field confined to the volume of resonators is the central question.

In this work, we show the spatial near-field distribution of optical resonances in broken-symmetry silicon (Si) metasurfaces imaged using PEEM with the help of a sub-monolayer potassium (K) layer covering the surface. Less than one atomic layer of potassium is sufficient to lower the work function and enables two-photon photoelectron emission using near-infrared (IR) light. We designed the broken-symmetry resonator array to host quasi-bound states in the continuum (quasi-BICs) with resonances in the near-IR.^{36,37,38} As the electromagnetic field is tightly confined in the body of the resonator, this quasi-BIC metasurface renders itself an ideal system to examine the near-field distribution using PEEM. By capturing photoelectron images of the optical modes at different resonant wavelengths and at various spatial locations across the metasurfaces, we show how the optical modes evolve spatially from the edges within our metasurfaces thereby corroborating the collective nature of quasi-BIC.³⁹ PEEM, therefore, offers versatile hyperspectral imaging of the near-field distribution while also maintaining both high spatial resolution and a large field of view—ideal for characterizing extended photonic modes in semiconductor photonic structures.

RESULTS & DISCUSSIONS:

Figure 1a shows the concept of photoelectron emission microscopy (PEEM). Photoelectron emission occurs in response to absorption of incident photons, and the photoelectron yield scales with the electromagnetic field intensity. Thus, the PEEM signal reveals the spatial distribution of electromagnetic fields by collecting the electrons emitted at all angles⁴⁰ from the sample upon far-field optical illumination. The electrons are then redirected onto a 2D imaging detector while preserving their spatial origin. Multiple photoelectron images can be sequentially acquired by scanning the excitation wavelength. The data is then compiled into a “spectral hypercube” data set, from which the photoelectron yield spectra, analogous to far-field optical absorption spectra, are extracted at each pixel of the PEEM data *post eventum*⁴¹ (see Methods section and Supplementary note for more information about the data acquisition and processing).

Photoemission requires that the energy gained by an electron from absorbed photons must exceed the work function of the sample’s host materials, as illustrated in Figure 1b. Thus, PEEM generally employs a deep UV or x-ray light source, which provides enough energy for the electrons to be extracted. However, in semiconductor metasurfaces designed for optical frequencies [from 3 eV (400nm) to 1.2 eV (1um)],⁴² the optical resonances are well below the work function of the resonator material and fall outside the energy range of traditional photoemission microscopy. For this reason, we rely here on multiphoton absorption processes at the optical resonance energies to generate photoelectrons for PEEM imaging. For Si metasurfaces designed for the near-IR, approximately four photons in the energy range of the optical modes would need to be absorbed by a single electron to overcome the material’s work function (see Figure 1b). A four-photon absorption process is impractical as the efficiency of this nonlinear process scales down for higher orders. Thus, the nonlinear photoelectron yield signal would be very weak, if not immeasurable.

To overcome this challenge, we find that depositing *in-situ* a sub-monolayer of potassium (K) on top of the metasurface lowers the material's work function to ~ 2.7 eV, which is sufficient to obtain photoelectron yield spectra via two-photon photoemission process using near-IR optical excitation [680 nm (~ 1.82 eV) to ~ 900 nm (~ 1.38 eV), see Supplementary Figure S1 for detail]. At these photon energies, we directly probe the metasurface's optical modes and observe their near-field distribution. As the intensity of two-photon photoemission is proportional to the square of the electromagnetic field intensity, PEEM images can be regarded as nonlinear maps of the near-field distribution of the optical fields.³² Furthermore, PEEM utilizes polarized far-field optical excitation, akin to typical optical experimental conditions, and a large excitation spot (tens of microns, see Methods section). The latter enables PEEM to access collective photonic modes supported by a metasurface and image many resonators simultaneously.

To showcase this approach, we designed and fabricated a Si metasurface with broken symmetry nanoresonators arranged in periodic arrays (Figure 1c). The metasurface is isolated from a gold-coated Si substrate by a 50 nm dielectric layer stack and coated by a thin (10nm) TiO_2 layer to prevent sample charging during PEEM measurements (see Sample fabrication in Methods section, and Supplementary Figure S2). Note the impacts of the TiO_2 film and the sub-monolayer of K to the optical properties of the metasurfaces are found to be minimal as described subsequently. This type of metasurface design exhibits narrowband quasi-BIC optical modes.^{27,43,44} Their existence can be explained through symmetry breaking operations performed on a metasurface with symmetries that guarantee true BIC.^{45,46} They appear as sharp resonance peaks in the reflectance spectra. Due to their high-quality factors at normal incidence excitation,⁴⁷ quasi-BICs are expected to result in significant enhancements of the photoemission process. Moreover, these modes are sensitive to input polarization⁴⁸ and their resonances are *collective modes*: *i.e.*, they depend on the location of the resonator within the entire resonator array that are being excited.³⁹ Thus, quasi-BIC are ideally suited to be studied using PEEM.

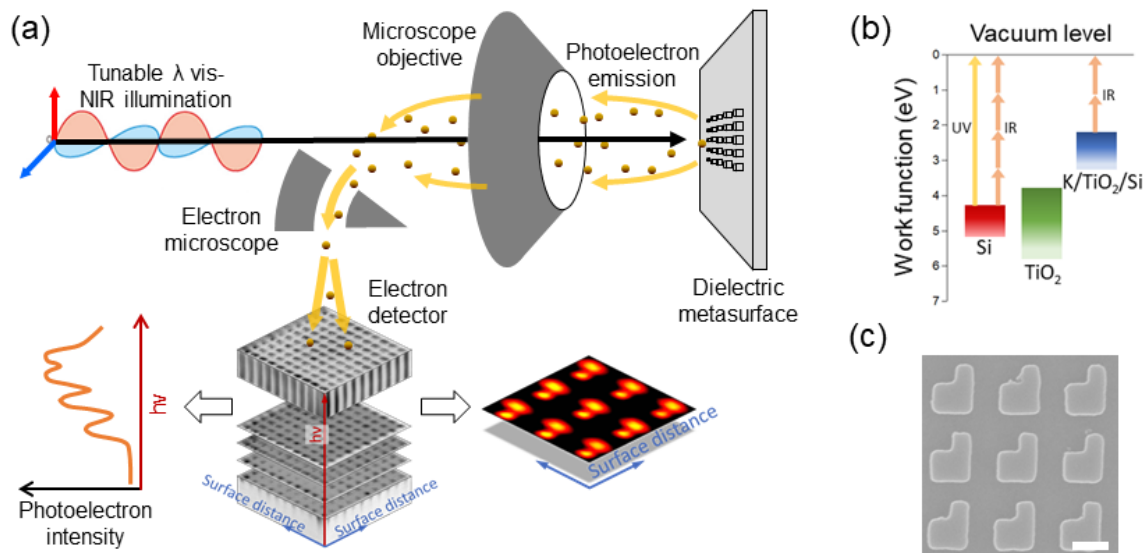


Figure 1: Schematic of the photoelectron emission microscope (PEEM). A Ti:S oscillator (for two-photon photoelectron excitation) and deep UV laser (for topographical imaging) are coupled to a photoelectron microscope. The emitted electron from the sample is then redirected onto a detector while maintaining its spatial

origin. The wavelength tunability of the Ti:S oscillator allows for acquiring two-dimensional photoelectron yield map as a function of the incident light wavelength. (b) Energy diagram of the various multiphoton processes and materials' work functions involved. (c) Scanning electron micrograph showing a few individual Si resonators that make up the larger metasurface. The scale bar is 250 nm.

In our Si metasurface, we find five resonances, labelled A, B, C, D (D1 and D2 for simulated), and E in the measured reflectance (Figure 2c) and the simulated absorption spectra (Figure 2b). The lower energy A- and B-peaks correspond to quasi-BICs with field distributions resembling that of out-of-plane magnetic and electric dipoles (MD_z , ED_z), respectively. The C-mode is a higher order magnetic dipole Mie mode with an antinode number $m = 2$ using dielectric rods notation. D1 corresponds to a $m = 2$ magnetic dipole and D2 to a higher order transverse electric (TE) mode with $m=2$. The spectra are presented for four incident polarization orientations, 0° , 45° , 90° , and 135° , depicted in Figure 2a. In Figure 2b and 2c, we observe that, for 45° incident polarization (green spectra), far-field excitation coupled strongly to the A- and C-peaks resonances of the metasurface whereas, for 135° incident polarization (orange spectra), the B- and D-peaks exhibit relative high intensity.

Assignment of the peaks between simulated and experimental results was initially based on peak positions and relative intensities, however because of some discrepancies in these characteristics, coupled with broadening in the experimental results, comparison between PEEM images and simulated profiles was used to confirm the final designations. Most notable is a blue shift of our resonances in the measured reflectance spectra. In addition, the simulation predicted a splitting of the D-peak, denoted as D1 and D2, which is not observed in our far-field reflectance measurements. We attributed this observation to the higher losses of our fabricated metasurface. We note that the reflectance spectra presented in Figure 2c is acquired from the same sample used in the PEEM measurement retrieved after annealing in the vacuum condition to remove surface K layer.

In Figure 2d, we show the photoelectron yield spectra of the metasurface extracted from multiple photoelectron images captured sequentially while varying the near IR excitation wavelengths. Throughout this manuscript, photoelectron yield or intensity is integrated over all electron kinetic energies. Image processing is used to subtract the background originating from the electron detector and correct for image distortion artifacts (more information is provided in Supplementary note, Analysis of PEEM data). We find that the photoelectron yield spectra correlate with the measured absorption (*i.e.*, $1 - \text{reflectance}$, Figure 2c) spectra, exhibiting the anticipated wavelength and polarization dependences for each optical resonance. For example, for 45° incident polarization (green spectra), the A- and C-peaks are the dominant features in Figure 2c and 2d. For 135° incident polarization (orange spectra), the A-peak is almost completely suppressed, and the B-peak is the most prominent feature. The peak positions in the photoelectron yield spectra are blue shifted by $\sim 1\%$ of the excitation energy. There is notable broadening of the respective linewidths in the photoelectron yield spectra (from a simulated $10 - 20$ meV to a measured $20 - 50$ meV full width at half maximum). These larger photoelectron linewidths might come from the broad spectral width of the Ti:S laser ($8 - 14$ meV across the excitation wavelength range used in the measurements), the variability in the size and shape of the resonators, and the increased loss due to the metallic K layer covering the surface. We also note that the PEEM spectra exhibits asymmetric peak shapes with tailing toward lower excitation energies, especially for low energy modes (*i.e.*, A and B-peaks). Consequently, the tail of the B-peak overlaps significantly with the A-peak, which we will discuss in the

subsequent section. Overall, we find a reasonable agreement between measured far-field absorption and the photoelectron yield spectra, validating that the spectra obtained using near-field PEEM imaging properly represents the Si metasurface response under an equivalent far-field optical excitation.

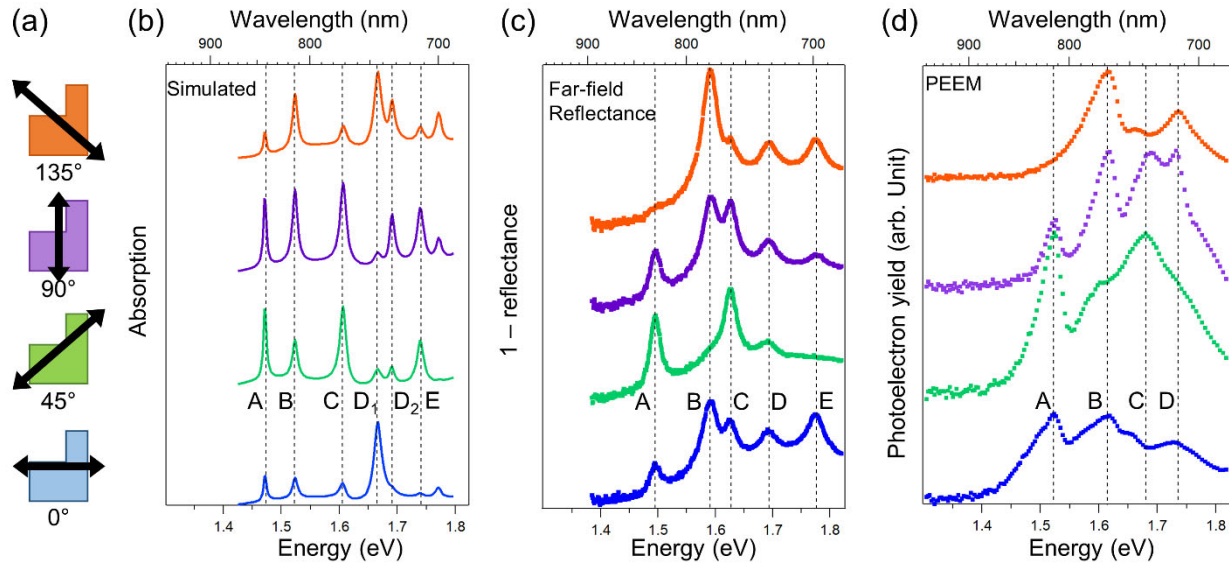


Figure 2: Comparison of metasurface absorption and photoelectron yield spectra. (a) Schematic excitation source polarization with respect to a single resonator. (b) Absorption spectra calculated using full-wave electromagnetic simulations (COMSOL). (c) Estimated absorption spectra of the Si metasurface measured with a home-built reflectance set-up. The sample used for this measurement was the same Si metasurface coated with TiO₂ and exposed to K during the PEEM measurements, before the reflectance measurements the sample was cleaned by annealing in UHV conditions. (d) Photoelectron yield spectra averaged over resonator's unit-cell area measured with PEEM. Spectra (b), (c), and (d) are presented for the selected orientations of the light polarization. The photonic modes are denoted as A (out of plane magnetic dipole quasi-BIC, MD_z), B (out of plane electric dipole quasi-BIC, ED_z), C (higher order magnetic dipole Mie mode with an antinode number $m = 2$), D ($m=2$ magnetic dipole), and higher order E assigned from the lower energy side.

We next describe the real-space imaging of the resonance processes based on PEEM imaging scheme. Figures 3a and 3b display large scale PEEM images of the Si metasurface acquired using deep UV (5.82 eV) and near IR (1.52 eV) excitation energies. While deep UV laser excitation (Figure 3a) renders the shapes of resonators very well in PEEM images (see Supplementary Figure S2 for a comparison with the resonator design), near IR laser excitation reveals information about the metasurface's near-field distribution via optical absorption. More specifically, we can visualize how well a resonator confines the electric field in the vicinity of its volume. Additional verification of the field confinement is provided in Supplementary Figure S4.

Figures 3c-f display averaged photoelectron yield images for a single resonator unit under near IR excitation close to the four resonance modes identified in Figure 2d at a 0° polarization angle. Here, we observe that the near-field photoelectron yield distribution is highly sensitive to excitation energy. These images are created by superimposing at least ten resonators within a single image to increase the statistics. For the A and B-peak resonances, the near-field distributions are highly symmetric as expected

for the out-of-plane MD_z and ED_z modes, respectively. Meanwhile, the C and D-peak resonances display non-symmetric and highly structured near-field distributions, as expected given the higher order of the modes. We note that the excitation energy used to generate the A-peak resonance image (1.42 eV, Figure 3c) is lower than the peak energy (1.52 eV) in Figure 2d. This is to minimize the contributions from the overlapping B mode (see Supplementary Figure S3a to S3d), which will be discussed in greater detail in the following paragraph.

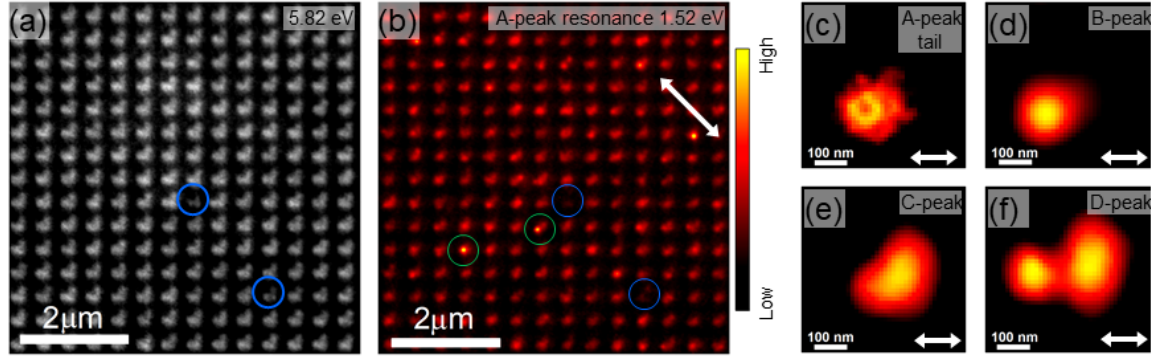


Figure 3: Excitation energy and polarization dependent nanoscale mode imaging. (a) and (b) Large field of view photoelectron intensity and yield images of the meta-surface array imaged using deep ultraviolet (5.82 eV, a) and A-peak photonic mode (1.52 eV, b) excitation energies. They illustrate the resonator-to-resonator intensity variations, high intensity spots in resonators (green circles), and inactive resonators (blue circles). (c), (d), (e), (f) Resonator averaged PEEM images with high statistics. The area in each image includes a repeating unit in both horizontal and vertical directions. The excitation energies are 1.42 eV (c), 1.62 eV (d), 1.65 eV (e), and 1.73 eV (f). Polarization directions are indicated by the white double arrows in (b), (c), (d), (e) and (f).

Next, we compare the near-field PEEM images to the calculated field distribution of the resonators. Figure 4a shows the near-field photoelectron yield distribution for excitation exactly at the A-peak resonance (1.52 eV) and a 45° polarization angle. We find that the signal is concentrated near the middle of the resonators, with an enhancement factor of five (in comparison to the area outside of the resonators), indicating the presence of an optical resonance. However, calculated electric field distributions for this mode, shown across three parallel planes slicing the middle, upper quartile, and near top-surface of the resonator (Figure 4b,c,d respectively), reveal that the electric fields for this out-of-plane magnetic dipole (MD_z) should form a ring-like mode profile concentrated near the center of the resonator volume that decays towards the surface. Though seemingly inconsistent, when the excitation energy is decreased to the lower energy tail of the A-peak (1.45 eV) a ring-like structure emerges (Figure 4e). Calculated electric field distributions below the A-peak resonance show the persistence of the ring-like MD_z mode profile (Figure 4f,g,h). This agreement leads us to interpret the absence of the MD_z ring-like structure in the PEEM images at the A-peak resonance to be a consequence of overlap between the A and B modes. This interpretation is supported by the poor peak separation that was previously noted in the photoelectron yield spectra (Figure 2d) and is further corroborated by the absence of any ring-like structure in PEEM images, even at the lower energy tail of the resonance, for 90° and 135° polarization angles where the A-peak has a low relative intensity with respect to the B-peak. We thus retrieve the near-field distribution associated with the first order quasi-BIC mode, characterized by an electric field resembling an out-of-

plane magnetic dipole (MD_z) mode inside the volume of each resonator.^{39,38} Similar observations can be made for the 0° incident polarization angle (Supplementary Figure S3a,b).

The near-field distribution of the B-peak resonance (1.61 eV) displays reasonable matching with the calculated electric field profiles expected for an out-of-plane electric dipole, ED_z (Figure 4i and 4j,k,l, respectively, for 45° polarization, and Supplementary Figure S3g,h,i,j for all polarizations). Like the A-peak resonance, the electric fields are weaker near the surface of the resonator and increase in intensity towards the center of the resonator volume with little change in their spatial distribution making it challenging to interpret whether the PEEM signal is originating from the surface or interior of the resonator. Overall, each polarization presented in this work (Figure S3g,h,i,j) shows a relatively intense B-peak resonance with reasonable agreement between the experimental near-fields and calculated electric fields.

The higher-order C and D-peak resonances (1.68 eV and 1.73 eV) show non-symmetric near-field distributions. This is displayed, for example, for the D-peak resonance at a 45° polarization angle in Figure 4m and all polarizations in supplementary Figures S3o,p,q,r. Importantly, the magnitude and spatial distribution of the calculated fields for these higher-order modes do not follow the trend of the lower-order A and B modes, and vary significantly as a function of height within the resonator (see Figure 4n,o,p and Supplementary Figure S3o,p,q,r for D-mode). Upon comparison to the calculated field distributions for the D-peak resonance at the middle, upper-quartile, and top height of the resonator (Figure 4n,o,p), the PEEM image does not closely resemble the field distribution at any single height. On the contrary, the near-field distribution of the PEEM image appears as a convolution of the fields across the volume of the resonators.

This “volumetric” sampling is counter intuitive for a photoemission process in general. The inelastic electron mean free paths of photoexcited electrons in silicon, TiO_2 , and K are supposedly on the order of a few nanometers or less.^{49,50} Given this circumstance, we expected the PEEM signal to originate primarily from the sub-monolayer of K at the top surface of a resonator. Yet, our work shows a depth sensitivity of the PEEM signal to electric fields within the Si resonators at a distance far beyond the anticipated escape depth of the electrons.^{51,52} The same correlations can be observed for both the C and D-peak resonances at other polarization angles in Supplementary Figure S3. It is worth noting that, for simplicity, we are comparing the projected 3D photoelectron data to 2D simulated near-field cross sections. It should be expected that the field profile taken at a single height of a resonator is unable to capture all the features of these optical resonances, adding to the disparity between simulated and calculated absorption spectra. Altogether, PEEM images of C and D-modes along with the calculated field profiles point to the sensitivity of photoelectron yield to the electric field confined to the volume of resonators.

PEEM images and corresponding simulated field profiles for all excitation energies of A to D-modes and incident polarizations, which are not included in Figure 4, can be found in Supplementary Figure S3.

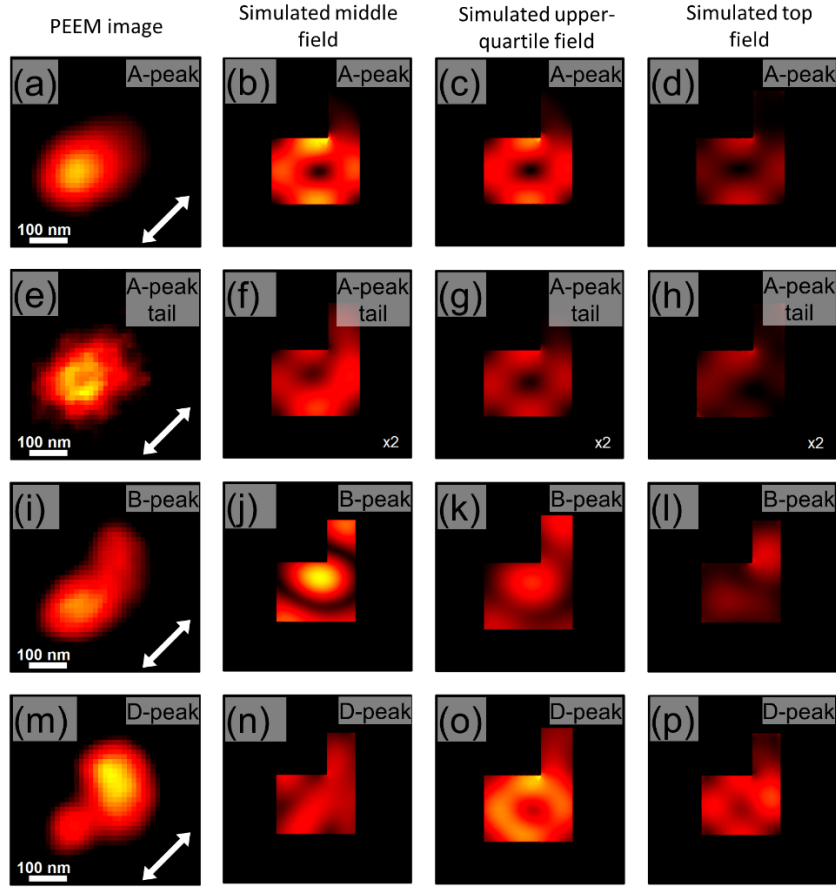


Figure 4: Excitation energy dependent nanoscale mode imaging and modelled field profiles of resonators for A, B, and D-peaks. (a), (e), (i), (m) Resonator averaged PEEM images with high statistics. The area in each image includes a single resonator unit-cell. The excitation energies are 1.52 eV (a), 1.45 eV (e), 1.60 eV (i), and 1.74 eV (m). Polarization directions are indicated by the white double arrows in (a), (e), (i), and (m). (b), (f), (j), (n) Modeled field distribution at the middle (in height) of the resonator. (c), (g), (k), (o) Modeled field distribution at the upper-quartile (in height) of the resonator. (d), (h), (l), (p) Modeled field distribution at the top (*i.e.*, surface) of the resonator. Each set of modeled field distributions (*i.e.*, top, upper-quartile, and middle for the same peak and polarization) are displayed on a shared color scale, (b), (c), and (d) for example. In addition, modeled field distributions for A-peak [(b), (c), (d)] and A-peak tail [(f), (g), (h)] also share the same color scale, though the fields in (f), (g), and (h) are multiplied by 2 to better view the contrasts. Note that in the simulated results the field of the areas outside the resonators were set 0.

As the formation of all photonic modes studied in this work involves neighboring resonators (*i.e.*, collective in nature), we anticipate the confinement of the electromagnetic field to vary as a function of distance from the array edge.³⁹ To examine this collective nature of quasi-BIC, we investigate the evolution of the photoelectron yield over the first few resonators near the array edge.

Figure 5a displays a photoelectron image for the corner of a large resonator array collected at the B-peak wavelength with 90° polarization angle. At the edges of the array (R1-R3, C1-C3), resonators in the top row (R1) and left-most column (C1) exhibit significantly enhanced intensity relative to their interior counterparts. We interpret this photoelectron intensity enhancement as a weakening of the quasi-BIC confinement due to lack of neighboring elements resulting in better in-coupling of light to these edge

resonators. We also note a strong suppression of the photoelectron intensity in the second column (C2) parallel to the incident polarization (*i.e.*, 90° polarization). This suppression in intensity is also apparent in the first row (R1) when the excitation polarization is parallel to the top edge (0° polarization) as shown in Figure S5a. The enhancement and suppression of intensity near edges vary with wavelength and are not equal for all optical resonances. When the photoelectron yield spectra are plotted as a function of position for columns (Figure 5b) or rows (Figure 5c), we find that the suppression observed in C2 occurs predominantly for the B-peak (see the black oval in Figure 5b) while the other resonance modes remain largely unchanged. This selective suppression is also observed for the B-peak in R2 when the polarization angle is parallel to the top edge (0° polarization, Figure S6b,c and the black oval therein).

As we transition (R3-R7, C3-C7) to the bulk region of the metasurface (R8 and above, C8 and above), we observe that evolution along the vertical edge shows an initial enhancement of the C-peak (C4 in Figure 5b), while evolution along the horizontal edge shows an initial enhancement of the D-peak (R4 in Figure 5c), before converging into the same relative intensities for the ‘bulk’ spectra (R8 and C8 in Figures 5c and 5b, respectively). These asymmetric dependences of the collective modes likely stem from the broken symmetry of the individual resonators.

Most importantly, from the evolution of the photoelectron yield spectra we conclude that approximately eight resonators, in both propagation directions, are necessary to fully establish the collective array modes, corroborating the result of previous work.^{19,39} After eight resonators, the spectral shape of the resonances closely matches that of the bulk array (Figure 2d) and any additional separation induces minimal spectral variation. Our data clearly supports the notion that the excited photonic modes of the resonators near the edges of the array are different from the photonic modes in the bulk (*i.e.*, the center of the array) of the metasurface. By capturing photoelectron yield spectra at each point of the image, PEEM uniquely enables us to draw such conclusions and study how these optical resonances forms within the metasurfaces.

As a side remark, we also found resonator to resonator variations in the photoelectron yield map due to the formation of additional “high intensity spots” along with “inactive” resonators. They are highlighted by the green and blue circles, respectively, in Figure 3a,b. The shape of the high intensity spots in Figure 3b resembles those of the resonant PEEM images of silver nanoparticles in ref. 22 that are uncontrollably agglomerated through the metal deposition process. This observation supports our speculation that the resonance high intensity spots appear from the imperfect side walls of the resonators due to the limited precision of the fabrication steps for the Si metasurfaces or due to clustered TiO₂ on resonator surfaces. As such, PEEM can also serve as a tool to diagnose heterogeneities and defected resonators of a metasurface and improve the engineering aspect of metasurface production.

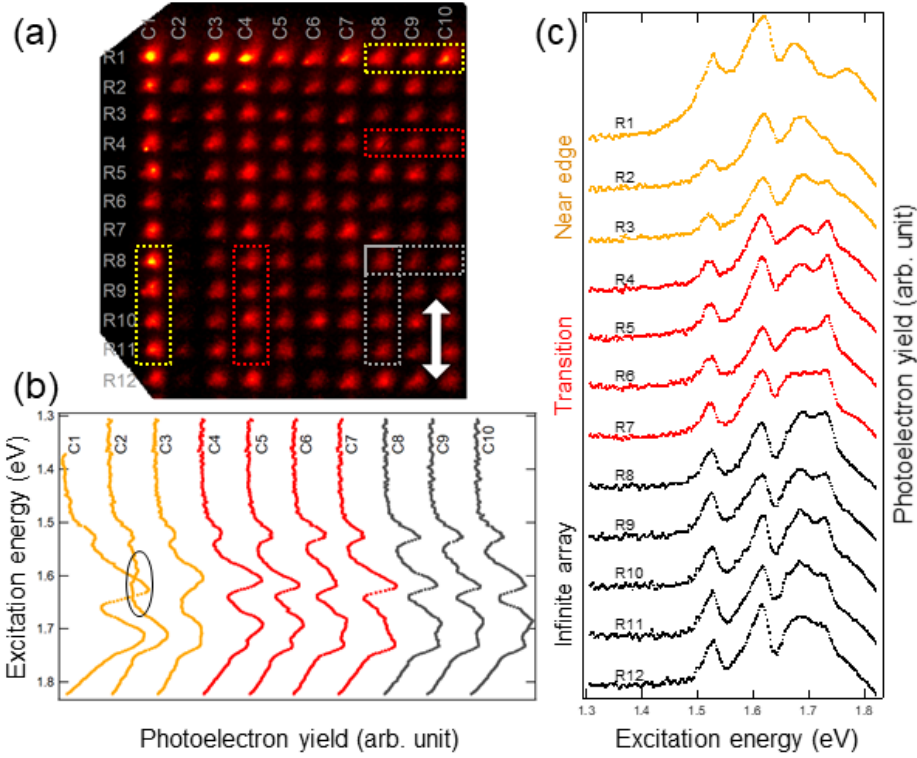


Figure 5: Evolution of the resonant quasi-BIC spectra from the edges to the middle of the resonator array. (a) Photoelectron image at 1.62 eV excitation at B-peak excitation. The resonators are designated as C1, ..., C10 and R1, ..., R12 within the image. The polarization direction is illustrated by the white double arrow. (b, c) The area averaged spectra of the resonators as a function of the distance from the vertical (b) and horizontal (c) edges. The spectra are averaged for 4 unit-cells along the column direction (b), and 3 unit-cells along the row direction (c) as indicated by the yellow, red, and grey dotted rectangles.

In summary, we presented concurrent spectroscopy and imaging of the near-field distribution of photonic modes in a Si metasurface using a high resolution, photoelectron-based imaging technique. The technique, photoelectron emission microscopy (PEEM), capitalizes on a far-field optical excitation with a “photon in, electron out” approach to probe the near-field enhancement of the electric fields through photoelectron yield. We exploit a less than one atom-thick surface layer of potassium and two-photon photoemission processes to concurrently realize near-infrared optical excitation and photoelectron imaging. In comparison to the modeled field distribution, photoelectron images represent the electromagnetic field emanating from the volume of the resonators, suitable to examine optical structures. We also show the dependence of these modes on input polarization and find that the coupling between eight resonators is needed to establish the quasi-BIC resonances. PEEM offers high spatial resolution with a relatively large field of view, proving its significance for studying photonic modes in semiconductor nanostructures and for diagnosing heterogeneities, such as defects or discontinuities, in nanophotonics.

METHODS:

Numerical simulation

Full-wave 3D electromagnetic calculation of the Si metasurface were performed using finite element method (COMSOL). Each model simulates a single resonator of dimension $\sim 270 \text{ nm} \times 210 \text{ nm}$, surrounded by periodic boundary condition. The lattice period is $\sim 412.5 \text{ nm}$.

Sample fabrication

The Si metasurface were fabricated using electron-beam lithography of polycrystalline Si films (300 nm thick), sputtered on a stack of Al_2O_3 (15nm), SiO_2 (30nm), Al_2O_3 (15nm) and Au (110nm) thin films, deposited on a Si wafer. The surface of the Si metasurface was then conformally coated with a 10nm-thick TiO_2 layer using atomic layer deposition (ALD). Both Au and TiO_2 were introduced to avoid sample charging during PEEM imaging due to their higher electric conductivities; we observed that metasurfaces fabricated on traditional Silicon-on-insulator substrate led to sample charging during PEEM imaging, which deteriorated the image quality.

We also verified that the deposition of the TiO_2 layer has minimal impact on the optical resonance properties of the Si metasurface based on reflectance measurement taken before and after the TiO_2 deposition. On some occasions, the resonance features of the Si metasurface sharpened after the TiO_2 deposition presumably due to the sample being heated during the ALD process, which may have improved the crystallinity of the sputtered Si.

Far-field reflectivity

We measure the linear spectra of the semiconductor metasurface using a homebuilt reflectance system. The sample used for this measurement was the same Si metasurface coated with TiO_2 and exposed to K during the PEEM measurements. However, before the Far-field reflectance measurements were acquired the sample was cleaned by annealing in UHV conditions. A polarized broadband white light emission from a thermal source is focused onto the sample using an achromatic lens of focal length 50mm. The scattered light, collected from the same lens, is then rerouted toward the entrance slit of a spectrometer. The low numerical aperture (0.2) of our imaging system limits the excitation angle of incident light, which preserves the quality factor of the quasi-BIC modes.

PEEM imaging

We conducted near-field imaging using a LEEM-III system (Elmitec Elektronenmikroskopie GmbH), operated in the photoelectron emission microscopy (PEEM) mode. Our PEEM instrument is connected to the output of a tunable near-IR Ti:Sapphire laser oscillator (normal incident, ~ 100 femtosecond pulse, Coherent Inc.), a deep ultraviolet (UV) laser (normal incident, 213 nm continuous wave, Toptica Photonics), and a deep UV-visible incoherent light source (incident angle of 73° relative to the sample surface normal, continuous wave, Energetiq Technology) with a Czerny–Turner monochromator (Acton Research Corporation). The UV and near-IR lasers are focused onto the sample surface (to spot sizes of 50 μm to 100 μm , respectively) using a fused silica lens of 750 mm focal length. The polarizations of the lasers are rotated with half waveplates. More details on the deep UV laser and the incoherent light sources can be found in Berg, *et al.*⁵³ and Sharma, *et al.*⁵⁴

The photoelectron yield spectra shown in Figure 2 are captured by changing the fundamental wavelength of the near infrared laser, and sequentially recording the photoelectron images, while maintaining the laser power constant for all wavelengths (typically 50 mW or less). The photoelectron yield spectra are then extracted from the specific pixel, or the pixels averaged in the data cube (illustrated in the lower left part of Fig. 1). We limit the laser power to be no more than 100 mW below which minimal space charge image degradation is found.⁵⁵

Prior to a PEEM measurement, the Si metasurface is loaded inside the PEEM instrument in an ultrahigh vacuum (base pressure 3×10^{-11} Torr in LEEM-III system), and then annealed overnight at $\sim 150^\circ\text{C}$ to remove water and other chemical species physisorbed from the air. Without unloading the sample, we then deposit no more than one atomic layer of potassium (K), provided by the alkali dispenser (SAES Getters S.p.A.) attached to the PEEM instrument while the pressure not exceeding $1-2 \times 10^{-10}$ Torr. Introducing K lowers the work function of the metasurface to ~ 2.7 eV. This value was determined via two independent measurements from the photoelectron onset using the deep UV incoherent light source (one-photon photoemission) and using the near-IR Ti:S laser (two-photon photoemission).

The ultrahigh vacuum ensures that the oxidation of K proceeds slowly such that the quality of K is preserved during the duration of the PEEM measurement, which is typically 2-3 hours and carried out at $\sim 5 \times 10^{-11}$ Torr. We do observe that potassium degrades over time under continuous laser exposure or leaving the sample overnight under vacuum. However, we found that annealing the metasurface to $\sim 150^\circ\text{C}$ for a few minutes, and then depositing another atomic layer of K maintains the superior image quality of the sample, as if K was deposited on freshly prepared metasurface samples.

SUPPORTING INFORMATION:

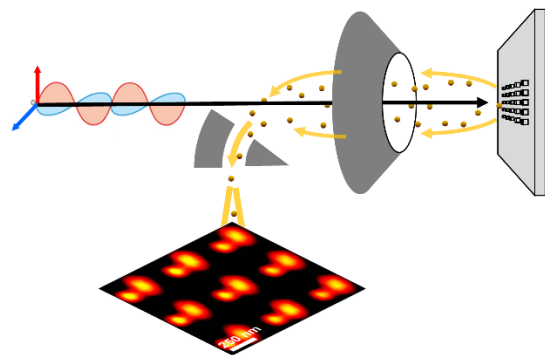
Additional description of PEEM data analysis, power dependence of photoelectron emission, detailed sample geometry, PEEM images and calculated field distributions for all polarizations and resonance peaks not shown in main text, two-color PEEM images showing resonance location with respect to resonator boundaries, spectral evolution of photoelectron yield as a function of distance from edge of the resonator array for 0° polarization angle, and videos showing PEEM images as a function of excitation energy for 0° and 45° polarizations

ACKNOWLEDGEMENT:

We thank P. Mantos, Amun Jarzembski, and G. Copeland for their measurement support. The work was supported by Sandia's LDRD program and in part by the US Department of Energy, Office of Basic Energy Sciences, Division of Materials Sciences and Engineering (grant BES 20-017574). The samples were fabricated, in part, at the Center for Integrated Nanotechnologies, an Office of Science User Facility operated for the US Department of Energy, Office of Science. Sandia National Laboratories is a multimission laboratory managed and operated by National Technology and Engineering Solutions of Sandia, LLC, a wholly owned subsidiary of Honeywell International, Inc., for the U.S. Department of Energy's National Nuclear Security Administration under contract DE-NA0003525. This paper describes objective technical results and analysis. Any subjective views or opinions that might be expressed in the paper do not necessarily represent the views of the U.S. Department of Energy or the United States Government.

This article has been authored by an employee of National Technology & Engineering Solutions of Sandia, LLC under Contract No. DE-NA0003525 with the U.S. Department of Energy (DOE). The employee owns all right, title and interest in and to the article and is solely responsible for its contents. The United States Government retains and the publisher, by accepting the article for publication, acknowledges that the United States Government retains a non-exclusive, paid-up, irrevocable, world-wide license to publish or reproduce the published form of this article or allow others to do so, for United States Government purposes. The DOE will provide public access to these results of federally sponsored research in accordance with the DOE Public Access Plan <https://www.energy.gov/downloads/doe-public-access-plan>.

For Table of Contents Only:



REFERENCES:

¹ Novotny, L.; van Hulst, N. Antennas for light, *Nature Photonics* 2011, 5, 83–90.

² Brener, I.; Liu, S.; Staude, I.; Valentine, J.; Holloway, C. Dielectric Metamaterials: Fundamentals, Designs and Applications; Woodhead Publishing, (2019).

³ Yablonovitch, E. Inhibited Spontaneous Emission in Solid-State Physics and Electronics, *Phys. Rev. Lett.* 1987, 58, 2059-2062.

⁴ Chen, X.; Zhang, Y.; Cai, G.; Zhuo, J.; Lai, K.; Ye, L. All-dielectric metasurfaces with high Q-factor Fano resonances enabling multi-scenario sensing, *Nanophotonics*, 2022, 11(20), 4537-4549.

⁵ Kamali, S. M.; Arbabia, E.; Arbab, A.; Faraon, A.; A review of dielectric optical metasurfaces for wavefront control; *Nanophotonics* 2018, 7(6), 1041-1068.

⁶ Genevet, P.; Capasso, F. Holographic optical metasurfaces: a review of current progress *Rep. Prog. Phys.* 2015, 78, 024401.

⁷ Krasnok, A.; Tymchenko, M.; Alu, A. Nonlinear Metasurfaces: A Paradigm Shift in Nonlinear Optics. *Materials Today* 2018, 21(1), 8-21.

⁸ Solntsev, A. S., Agarwal, G. S. & Kivshar, Y. S. Metasurfaces for quantum photonics. *Nat. Photonics*, 2021, 15, 327–336.

⁹ Santiago-Cruz, T.; Gennaro, S. D.; Mitrofanov, O.; Addamane, S.; Reno, J.; Brener, I.; Chekhova, M. V. Resonant metasurfaces for generating complex quantum states, *Science*, 2022, 377, 6609, 991-995.

¹⁰ Gennaro, S. D.; Sonnefraud, Y.; Verellen, N.; Van Dorpe, P.; Moshchalkov, V.V.; Maier, S. A.; Oulton, R. F. Spectral interferometric microscopy reveals absorption by individual optical nanoantennas from extinction phase, *Nature Communications* 2014, 5, 3748.

¹¹ Mack, D. L.; Cortés, E.; Giannini, V.; Török, P.; Roschuk, T.; Maier, S. A. Decoupling absorption and emission processes in super-resolution localization of emitters in a plasmonic hotspot, *Nature Communications* 2017, 8, 14513.

¹² Simoncelli, S.; Li, Y.; Cortés, E.; Maier, S. A. Imaging Plasmon Hybridization of Fano Resonances via Hot-Electron-Mediated Absorption Mapping, *Nano Lett.* 2018, 18, 6, 3400–3406.

¹³ Habteyes, T. G.; Staude, I.; Chong, K. E.; Dominguez, J.; Decker, M.; Miroshnichenko, A.; Kivshar, Y. and Brener, I. Near-field mapping of optical modes on all-dielectric silicon nanodisks. *ACS Photonics*, 2014, 1(9), pp.794-798.

¹⁴ Tamagnone, M.; Ambrosio, A.; Chaudhary, K.; Jauregui, L. A.; Kim, P.; Wilson, W. L.; Capasso, F. Ultra-confined mid-infrared resonant phonon polaritons in van der Waals nanostructures, *Sci. Adv.* 2018, 4, eaat7189.

¹⁵ Yin, L.; Vlasko-Vlasov, V. K.; Rydh, A.; Pearson, J.; Welp, U.; Chang, S.-H.; Gray, S. K.; Schatz, G. C.; Brown, D. B.; Kimball, C. W. Surface plasmons at single nanoholes in Films, *Appl. Phys. Lett.* 2004, 85, 467.

¹⁶ Coenen, T.; van de Groep, J.; Polman, A. Resonant Modes of Single Silicon Nanocavities Excited by Electron Irradiation, *ACS Nano* 2013, 7, 1689–1698.

¹⁷ Van De Groep, J.; Coenen, T.; Mann, S. A.; Polman, A. Direct imaging of hybridized eigenmodes in coupled silicon nanoparticles, *Optica*, 2016, 3, 93-99.

¹⁸ Peng, S.; Schilder, N. J.; Ni, X.; van de Groep, J.; Brongersma, M. L.; Alu, A.; Khanikaev, A. B.; Atwater, H. A.; Polman, A. Probing the Band Structure of Topological Silicon Photonic Lattices in the Visible Spectrum, *Phys. Rev. Lett.* 2019, 117401.

¹⁹ Dong, Z.; Mahfoud, Z.; Paniagua-Domínguez, R.; Wang, H.; Fernández-Domínguez, A. I.; Gorelik, S.; Ha, S. T.; Tjiptoharsono, F.; Kuznetsov, A. I.; Bosman, M.; Yang, J. K. W. Nanoscale mapping of optically inaccessible bound-states-in-the-continuum, *Light: Science & Applications*, 2022, 11, 20.

²⁰ Kociak, M.; Ste'phan, O. Mapping plasmons at the nanometer scale in an electron microscope, *Chem. Soc. Rev.*, 2014, 43, 3865-3883.

²¹ Polman, A.; Kociak, M.; García de Abajo, F. J. Electron-beam spectroscopy for nanophotonics, *Nature Mater.*, 2019, 1158, 1158–1171.

²² Kubo, A.; Onda, K.; Petek, H.; Sun, Z.; Jung, Y. S.; Kim, H. K. Femtosecond Imaging of Surface Plasmon Dynamics in a Nanostructured Silver Film, *Nano Lett.* 2005, 5, 6, 1123–1127.

²³ Cinchetti, M.; Gloskovskii, A.; Nepjiko, S. A.; Schönhense, G.; Rochholz, H.; Kreiter, M., Photoemission Electron Microscopy as a Tool for the Investigation of Optical Near Fields, *Phys. Rev. Lett.*, 2005, 95, 047601.

²⁴ Thomas, S; Thomas, R.; Zachariah, A. K.; Kumar, R.; Mishra, R. K., Thermal and Rheological Measurement Techniques for Nanomaterials Characterization, Elsevier, 2017.

²⁵ Kubo, A.; Onda, K.; Petek, H.; Sun, Z.; Jung, Y. S.; Kim, H. K. Femtosecond Imaging of Surface Plasmon Dynamics in a Nanostructured Silver Film, *Nano Lett.* 2005, 5, 6, 1123–1127.

²⁶ Zhang, L.; Kubo, A.; Wang, L.; Petek, H.; Seideman, T., Imaging of surface plasmon polariton fields excited at a nanometer-scale slit, *Phys. Rev. B*, 2011, 84, 245442.

²⁷ Kahl, P.; Wall, S.; Witt, C.; Schneider, C.; Bayer, D.; Fischer, A.; Melchior, P.; Horn-von Hoegen, M.; Aeschlimann, M.; Meyer zu Heringdorf, F. J. Normal-Incidence Photoemission Electron Microscopy (NI-PEEM) for Imaging Surface Plasmon Polaritons, *Plasmonics*, 2014, 9, 1401–1407.

²⁸ Bauer, E. *Surface Microscopy with Low Energy Electrons*, Springer New York, 2014.

²⁹ Hüfner, S. *Photoelectron Spectroscopy - Principles and Applications*, Springer-Verlag Berlin Heidelberg, 2003.

³⁰ Zhang, L.; Kubo, A.; Wang, L.; Petek, H.; Seideman, T. Imaging of surface plasmon polariton fields excited at a nanometer-scale slit, *Phys. Rev. B*, 2011, 84, 245442.

³¹ Gong, Y.; Joly, A. G.; El-Khoury, P. Z.; Hess, W. P. Nonlinear Photoemission Electron Micrographs of Plasmonic Nanoholes in Gold Thin Films, *J. Phys. Chem. C* 2014, 118, 25671-25676.

³² Yu, H.; Sun, Q.; Ueno, K.; Oshikiri, T.; Kubo, A.; Matsuo, Y.; Misawa, H. Exploring Coupled Plasmonic Nanostructures in the Near Field by Photoemission Electron Microscopy, *ACS Nano* 2016, 10, 11, 10373–10381.

³³ Fitzgerald, J. P. S.; Word, R. C.; Saliba, S. D.; Könenkamp, R., Photonic near-field imaging in multiphoton photoemission electron microscopy, *Phys. Rev. B*, 2013, 87, 205419.

³⁴ Hartmann, H.; Barke, I.; Friedrich, A.; Plötz, P.-A.; Bokareva, O. S.; Bahrami, M.; Oldenburg, K.; Elemans, J. A. A. W.; Irsig, R.; Meiwas-Broer, K.-H.; Kühn, O.; Lochbrunner, S.; Speller, S., Mapping Long-Lived Dark States in Copper Porphyrin Nanostructures, *J. Phys. Chem. C* 2016, 120, 30, 16977–16984.

³⁵ Stallberg, K.; Lilienkamp, G.; Daum, W., Plasmon–Exciton Coupling at Individual Porphyrin-Covered Silver Clusters, *J. Phys. Chem. C* 2017, 121, 25, 13833–13839.

³⁶ Hsu, C. W.; Zhen, B.; Stone, A. D.; Joannopoulos, J. D.; Soljacic, M. Bound states in the continuum, *Nature Reviews Materials*, 2016, 1, 16048.

³⁷ Koshelev, K.; Lepeshov, S.; Liu, M.; Bogdanov, A.; Kivshar, Y., Asymmetric Metasurfaces with High-Q Resonances Governed by Bound States in the Continuum, *Phys. Rev. Lett.*, 2018, 121, 193903.

³⁸ Koshelev, K.; Bogdanov, A.; Kivshar, Y., Engineering with Bound States in the Continuum, *Optics and Photonics News*, 2020, 31, 38-45.

³⁹ Campione, S., Liu, S., Basilio, L.I., Warne, L.K., Langston, W.L., Luk, T.S., Wendt, J.R., Reno, J.L., Keeler, G.A., Brener, I. and Sinclair, M.B. Broken symmetry dielectric resonators for high quality factor Fano metasurfaces. *ACS Photonics*, 2016, 3(12), 2362-2367.

⁴⁰ We note that the high voltage applied between the sample and the PEEM objective lens enables us to collect electrons emitted from all angles.

⁴¹ Genco, A.; Cruciano, C.; Corti, M.; McGhee, K. E.; Ardini, B.; Sortino, L.; Huttenhofer, L.; Virgili, T.; Lidzey, D. G.; Maier, S. A.; Bassi, A.; Valentini, G.; Cerullo, G.; Manzoni, C. k-Space Hyperspectral Imaging by a Birefringent Common-Path Interferometer, *ACS Photonics* 2022, 9, 3563-3572.

⁴² Staude, I.; Schilling, J. Metamaterial-inspired silicon nanophotonics, *Nature Photonics* 2017, 11, 274–284.

⁴³ Podbiel, D.; Kahl, P.; Makris, A.; Frank, B.; Sindermann, S.; Davis, T. J.; Giessen, H.; Horn-von Hoegen, M.; Meyer zu Heringdorf, F. J. Imaging the Nonlinear Plasmoemission Dynamics of Electrons from Strong Plasmonic Fields, *Nano Lett.* 2017, 17, 6569-6574.

⁴⁴ Davis, T. J.; Janoschka, D.; Dreher, P.; Frank, B.; Meyer zu Heringdorf, F. J.; Giessen, H. Ultrafast vector imaging of plasmonic skyrmion dynamics with deep subwavelength resolution, *Science* 2020, 368, 386.

⁴⁵ Plotnik, Y.; Peleg, O.; Dreisow, F.; Heinrich, M.; Nolte, S.; Szameit, A.; Segev, M. Experimental Observation of Optical Bound States in the Continuum, *Phys. Rev. Lett.* 2011, 107, 183901.

⁴⁶ Cerjan, A.; Jörg, C.; Vaidya, S.; Augustine, S.; Benalcazar, W. A.; Hsu, C. W.; von Freymann, G.; Rechtsman, M. C. Observation of bound states in the continuum embedded in symmetry bandgaps, *Sci. Adv.* 2021, 7, eabk1117.

⁴⁷ Liu, S.; Vaskin, A.; Addamane, S.; Leung, B.; Tsai, M. C.; Yang, Y.; Vabishchevich, P. P.; Keeler, G. A.; Wang, G.; He, X.; Kim, Y.; Hartmann, N. F.; Htoon, H.; Doorn, S. K.; Zilk, M.; Pertsch, T.; Balakrishnan, G.; Sinclair, M. B.; Staude, I.; Brener, I. Light-Emitting Metasurfaces: Simultaneous Control of Spontaneous Emission and Far-Field Radiation, *Nano Lett.* 2018, 18, 11, 6906–6914.

⁴⁸ Overvig, A. C.; Malek, S. C.; Carter, M. J.; Shrestha, S.; Yu, N. Selection rules for quasibound states in the continuum, *Phys. Rev. B* 2020, 102, 035434.

⁴⁹ Tanuma, S.; Powell, C. J.; Penn, D. R., Calculations of electron inelastic mean free paths. II. Data for 27 elements over the 50–2000 eV range, *Surface & Interface Analysis*, 1991, 17, 13, 911-926.

⁵⁰ Kuhr, J. C.; Fitting, H. J. Monte Carlo simulation of electron emission from solids, *Journal of Electron Spectroscopy and Related Phenomena*, 1999, 105, 2–3, 257-273.

⁵¹ Berg, M.; Liu, F.; Smith, S.; Copeland, R. G.; Chan, C. K.; Mohite, A. D.; Beechem, T. E.; Ohta, T. Imaging atomically thin semiconductors beneath dielectrics via deep ultraviolet photoemission electron microscopy, *Phys. Rev. Applied*, 2019, 12, 064064.

⁵² Beechem, T. E.; Smith, S. W.; Copeland, R. G.; Liu, F.; Ohta, T. Spectral and Polarization Based Imaging in Deep-Ultraviolet Excited Photoelectron Microscopy, *Review of Scientific Instruments*, 2022, 93, 053701.

⁵³ Berg, M.; Keyshar, K.; Bilgin, I.; Liu, F.; Yamaguchi, H.; Vajtai, R.; Chan, C.; Gupta, G.; Kar, S.; Ajayan, P.; Ohta, T.; Mohite, A. D. Layer dependence of the electronic band alignment of few-layer MoS₂ on SiO₂ measured using photoemission electron microscopy, *Phys. Rev. B* 2017, 95, 235406.

⁵⁴ Sharma, P. A.; Ohta, T.; Brumbach, M.; Sugar, J. D.; Michael, J. R. Ex Situ Photoelectron Emission Microscopy of Polycrystalline Bismuth and Antimony Telluride Surfaces Exposed to Ambient Oxidation, *ACS Applied Materials & Interfaces*, 2021, 13, 18218-18226.

⁵⁵ Buckanie, N. M.; Gőöhre, J.; Zhou, P.; von der Linde, D.; Horn-von Hoegen, M.; Meyer zu Heringdorf, F.-J. Space charge effects in photoemission electron microscopy using amplified femtosecond laser pulses, *J. Phys.: Condens. Matter* 2009, 21, 314003.

Supporting information: Near-field Imaging of Optical Resonance Modes in Si Metasurfaces Using Photoelectron Microscopy

Alex Boehm¹, Sylvain D. Gennaro^{1,2}, Chloe F. Doiron^{1,2}, Thomas E. Beechem³, Michael B. Sinclair¹, Igal Brener^{1,2}, Raktim Sarma^{1,2}, Taisuke Ohta^{1*}

1 Sandia National Laboratories, Albuquerque, NM 87185

2 Center for Integrated Nanotechnologies, Albuquerque, NM 87185

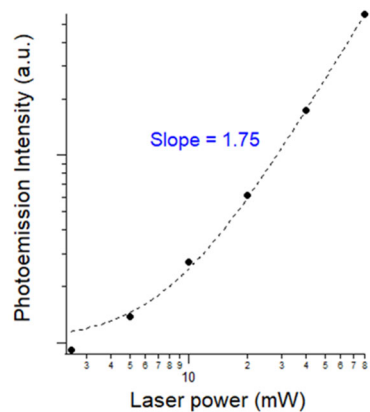
3 School of Mechanical Engineering and Birck Nanotechnology Center, Purdue University, West Lafayette, IN 47907

Supplementary note: Analysis of PEEM data

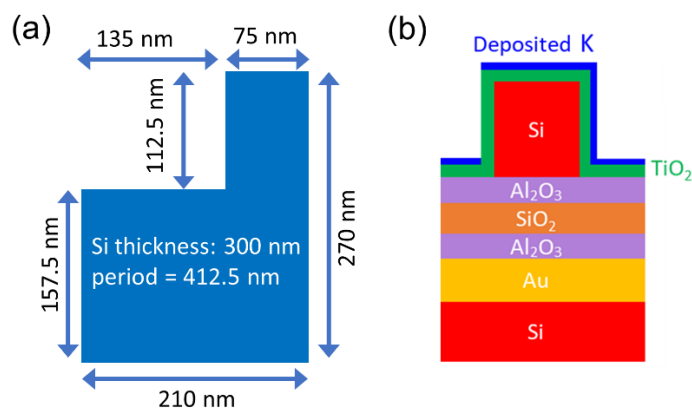
Photoelectron image datasets (*i.e.*, the data cube either as a function of the excitation wavelength or the polarization orientation) were processed to eliminate the impacts of (1) the two-dimensional electron detector's inhomogeneous response, (2) the photoelectron cross section as a function of the excitation wavelength, (3) the image distortion originating from the imperfect alignment of the electron optics, as well as (4) the gradual loss of photoelectron intensity with time that comes from prolonged exposure of the samples to intense visible to near IR pulse laser irradiation. We presume that the heating of the sample due to pulse laser exposure causes the slow K loss, and hence increases the work function of the sample gradually. For (1), we first acquired an image of an area where the sample surface is homogeneous. This reference image was used to correct the inhomogeneous response of the electron detector. For (2), the photoelectron cross section variation due the excitation wavelength was considered by normalizing with the photoelectron intensity variations of the uniform area adjacent to the resonator arrays as a function of the excitation wavelength or the polarization orientation. To eliminate the image distortion (3), we aligned the resonator arrays as if the resonator locations form a perfect orthogonal grid. We found that the distortion within the field of view amounts as much as 20 pixels within a 600 pixel \times 600 pixel image (with \sim 12.5 nm/pixel) depending on the alignment of the electron optics. For (4), the gradual loss of the photoelectron intensity was corrected by acquiring two iterations of the wavelength sweep, or of the polarization sweep, and linearly interpolating such that the intensities of the identical features and the baseline in the two consecutive sweeps have the same photoelectron intensity. This process also allows correcting for the sample's spatial drift during the data acquisition.

We note that the PEEM data in this work is presented in the unit of the photoelectron yield. For the visible to near IR excitation data, we applied a square-root to the photoelectron intensity to obtain the photoelectron yield accounting for the two-photon photoemission process.¹ The exposure time of the detector and the laser power are kept constant for all data presented here. The photoelectron yield spectra are averaged over the unit-cell area of the resonator array unless specified otherwise.

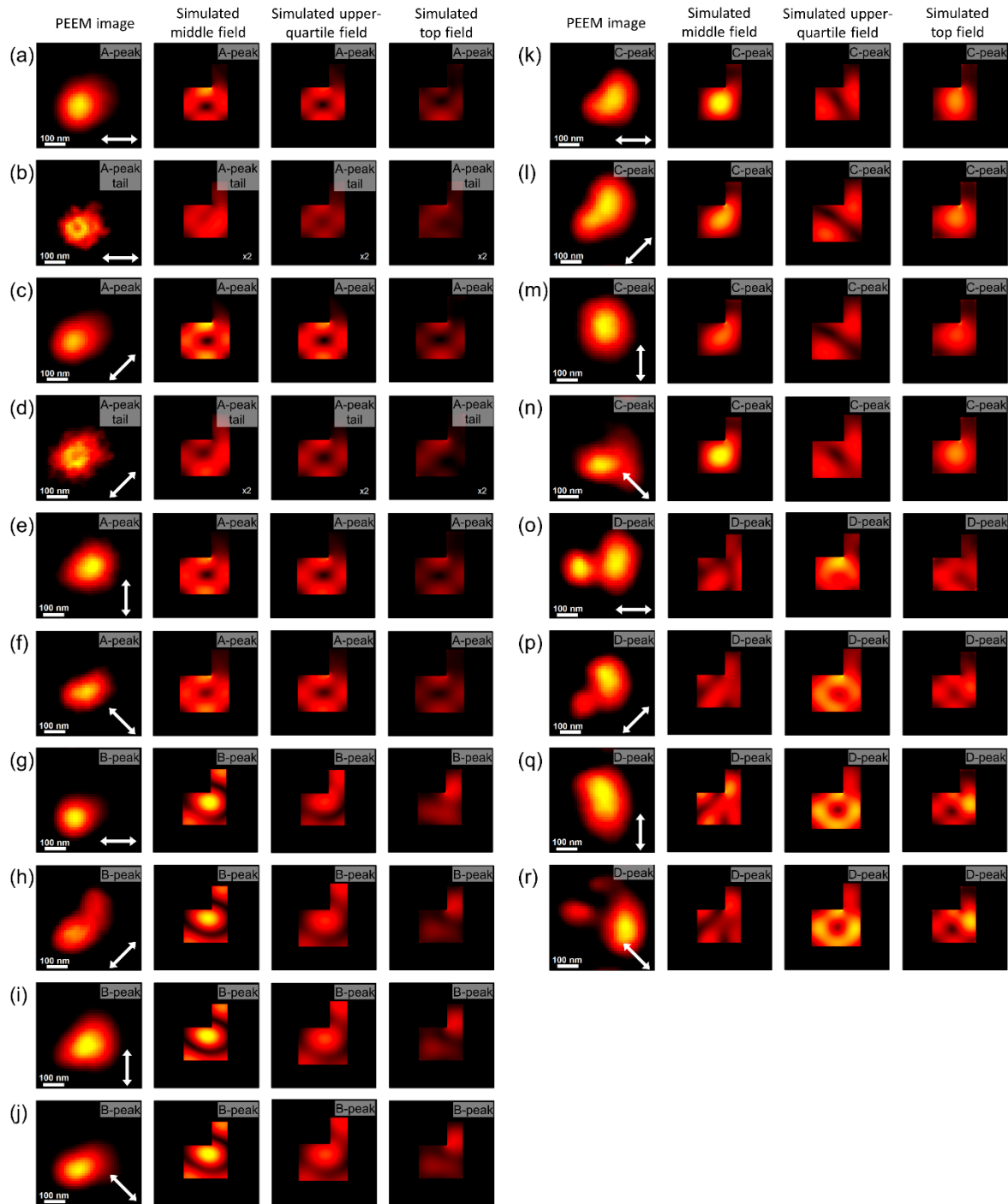
We capture multiple photoelectron yield spectra under short exposure and averaged them over the repeating unit-cell area of a single resonator. We note that the resonators near the edges of the arrays are excluded in these averaged spectra owing to the edge effects addressed within the main portion of the manuscript.



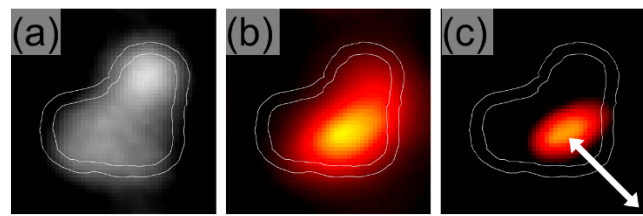
Supplementary Figure S1: Power dependence of the photoelectron emission showing close to 2-photon photoemission process.



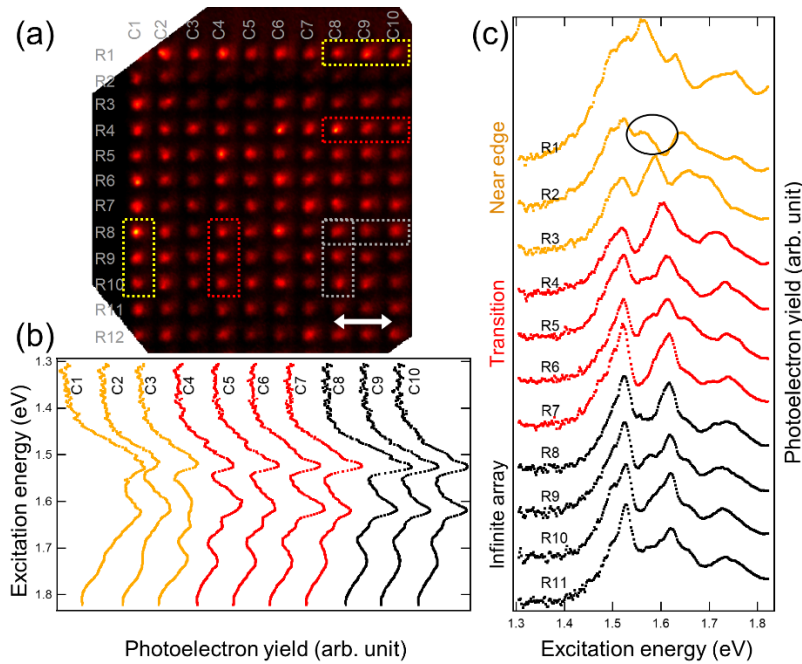
Supplementary Figure S2: Detailed geometry of the resonator array design used in photoelectron imaging of the metasurfaces. (a) Detailed dimensions of the resonator. (b) 2D cross-sectional schematic of the sample architecture.



Supplementary Figure S3: Excitation energy and polarization dependent nanoscale mode imaging and simulation. Average PEEM image of a resonator unit cell area (1st column), simulated field distribution at the middle of the resonators (2nd column), simulated field distribution at the upper-quartile (in height) of the resonators (3rd column), and simulated field distribution at the top of the resonators (4th column) collected at or near A-peak resonance (a), (b), (c), (d), (e), (f), at B-peak resonance (g), (h), (i), (j), at C-peak resonance (k), (l), (m), (n), and at D-peak resonance (o), (p), (q), (r). Each set of modeled field distributions (*i.e.*, top, upper-quartile, and middle for the same peak and polarization) are displayed on a shared color scale, except for (b) and (d) that share color scales with (a) and (c) respectively. Polarization direction is illustrated by the white double arrow.



Supplementary Figure S4: Two-color illumination imaging [6.44 eV and 1.61 eV (*i.e.*, B-peak) excitations] showing the resonance location with respect to the resonator geometry. (a) 6.44 eV illumination only. (b) 6.44 eV and 1.61 eV co-illumination. (c) 1.61 eV illumination only. Solid double lines illustrate the approximate locations of the resonator boundaries extracted from (a) and highlight the resonance location of the B-mode. The polarization for the 1.61 eV illumination is 135° illustrated by the white double end arrow (see Fig. 2 for the definition of the polarization orientation). 6.44 eV illumination (unpolarized) is carried out with an incident angle of 73° off-normal to the sample and using a Xe-lamp with a monochromator.



Supplementary Figure S5: Evolution of the resonant BIC spectra from the edges to the middle of the resonator array similar to Fig. 4, but with 0° polarization. (a) Photoelectron image at 1.61 eV excitation. The resonators are designated as C1, ..., C10 and R1, ..., R12 within the image. The polarization direction is 0° and is illustrated by the white double arrow. (b) and (c) The area averaged spectra of the resonators as a function of the distance from the vertical (b) and horizontal (c) edges. The spectra are averaged for 3 unit cells along the column direction (b), and 3 unit cells along the row direction (c) as indicated by the yellow dotted rectangles for the C1 and R1 spectra.

¹ Stenmark, T.; Könenkamp, R. Photoemission electron microscopy to characterize slow light in a photonic crystal line defect, Phys. Rev B 2019, 99, 205428.